The 3-dimensional Einstein–Klein–Gordon system in characteristic numerical relativity

W. Barreto,[1] A. Da Silva,[2] R. Gómez,[3,4] L. Lehner,[2] L. Rosales,[5] and J. Winicour[6,4]

[1] *Centro de Física Fundamental, Facultad de Ciencias, Universidad de los Andes, Mérida, Venezuela.*
[2] *Department of Physics and Astronomy, 2002 Nicholson Hall, Louisiana State University, Baton Rouge, LA 70803-4001.*
[3] *Pittsburgh Supercomputing Center, 4400 Fifth Avenue, Pittsburgh, PA 15213.*
[4] *Department of Physics and Astronomy, University of Pittsburgh, Pittsburgh, PA 15260.*
[5] *Universidad Experimental Politécnica "Antonio José de Sucre", Puerto Ordaz, Venezuela.*
[6] *Max-Planck-Institut für Gravitationsphysik, Albert-Einstein-Institut, 14476 Golm, Germany.*

(Dated: December 14, 2004)

We incorporate a massless scalar field into a 3-dimensional code for the characteristic evolution of the gravitational field. The extended 3-dimensional code for the Einstein–Klein–Gordon system is calibrated to be second order convergent. It provides an accurate calculation of the gravitational and scalar radiation at infinity. As an application, we simulate the fully nonlinear evolution of an asymmetric scalar pulse of ingoing radiation propagating toward an interior Schwarzschild black hole and compute the backscattered scalar and gravitational outgoing radiation patterns. The amplitudes of the scalar and gravitational outgoing radiation modes exhibit the predicted power law scaling with respect to the amplitude of the initial data. For the scattering of an axisymmetric scalar field, the final ring down matches the complex frequency calculated perturbatively for the $\ell = 2$ quasinormal mode.

PACS numbers: 04.40.-b, 04.25.Dm, 04.40.Nr, 04.40.Dg

I. INTRODUCTION

Numerical relativity has made significant advances in simulations which will be helpful toward achieving the final goal of providing useful information for the detection of gravitational waves, although the goal of achieving long term simulations of binary black holes has not yet been met. At some level, we have entered an era in which Einstein's equations can effectively be considered solved at the local level; i.e. there are several codes which provide accurate evolutions in a sufficiently small space-time region where the gravitational field has small variation when expressed in a Riemann normal coordinate system. However, at the global level, the computation of gravitational radiation from black hole space-times remains a highly challenging problem, in which there are vastly different time scales at play in the inner and outer regions and in which the proper choice of gauge is far from obvious.

Most work in numerical relativity is based upon the Cauchy $3+1$ formalism (see, for instance [1]). A different approach, which is specifically tailored to study radiation, is based upon the characteristic initial value problem. This approach, which has been successful in computing gravitational radiation in single black hole space-times, is the focus of attention in this paper.

Bondi, Sachs and Penrose [2, 3, 4] have proposed formalisms to deal with radiation which today are the cornerstones for the characteristic numerical formulation of general relativity. All schemes for characteristic evolution have a common structure. The main ingredient is the space–time foliation by null hypersurfaces $u =$ constant, generated by a set of bi–characteristic null rays x^A, with a coordinate λ varying along them. In null coordinates $(u,\ \lambda,\ x^A)$ the main set of Einstein's equations has the form

$$F_{,\lambda} = H_F[F,G], \tag{1}$$
$$G_{,u\lambda} = H_G[F,G], \tag{2}$$

where F represents variables intrinsic to a single null hypersurface u, G represents the evolution variables and, H_F and H_G are nonlinear operators intrinsic to the null hypersurface u. Besides these main equations, there is a set of constraint equations which are satisfied via the Bianchi identities if they are satisfied on an inner boundary. At null infinity, these constraints can be interpreted as conservation conditions governing energy and angular momentum.

The numerical implementation of the characteristic method consists in evolving a given field (e.g. scalar, electromagnetic or gravitational) on a family of null hypersurfaces along a discrete sequence of retarded time steps. A stable, second order accurate, fully nonlinear, 3-dimensional code (the PITT code) has been based upon this characteristic formalism. Its implementation, tests and results have been presented in a series of papers [5, 6, 7, 8, 9]. The code poses data on an initial null hypersurface and on an inner worldtube boundary, and evolves the exterior space-time

out to a compactified version of null infinity. The code calculates waveforms at null infinity [9, 10], tracks a dynamical black hole and excises its internal singularity from the computational grid [11, 12].

The PITT code uses an explicit finite difference evolution algorithm based upon retarded time steps on a uniform 3–dimensional null coordinate grid [9, 10]. A crucial ingredient of the code is the $\eth$–module [6] which incorporates a computational version of the Newman–Penrose $\eth$-formalism [13]. The $\eth$-module covers the sphere with two overlapping stereographic coordinate grids (North and South). It provides everywhere regular, second order accurate, finite difference expressions for tensor fields on the sphere and their covariant derivatives. The $\eth$–calculus simplifies the underlying equations, avoids spurious coordinate singularities and allows accurate differentiation of tensor fields on the sphere in a computationally efficient and clean way. The approach leads to a straightforward implementation of a second order convergent, finite difference code. The PITT code has undergone recent improvements to increase the accuracy in the simulation of highly distorted single black hole space-times [8] and in the calculation of the Bondi news function which describes the radiated waveform at null infinity $\mathcal{I}^+$ [14, 15]. The characteristic code has been extended to include a naive hydrodynamical treatment, which has been applied to model a fluid ball falling into a Schwarzschild black hole [16] and to model a polytrope in orbit near a Schwarzschild black hole [17].

Our work here is motivated by the possibility of using characteristic evolution to model bosonic stars in orbit about a black hole. Besides the possible importance of such stars astrophysical and cosmological aspects [18, 19, 20], their existence as solitonic solutions [21, 22, 23] offers a way to model a compact object without the difficulties of a hydrodynamic description of the matter field. The bosonic field can be evolved using the same characteristic techniques developed for the gravitational field. With this goal in mind, here we incorporate a scalar field in the PITT code. We demonstrate that the code provides a stable, convergent evolution of a 3-dimensional massless Einstein–Klein–Gordon (EKG) system in the region exterior to a black hole.

This extension also allows the study of the nonlinear interaction between gravitational and scalar radiation in a fully 3-dimensional black hole space-time. Previous studies have measured the nonlinear effects in the scattering of a gravitational wave off a black hole, using codes based upon characteristic evolution [9, 24] and upon Cauchy evolution [25, 26]. In the purely gravitational case, the spherical harmonic modes of the gravitational waves are mixed by quadratic (and higher order) interactions. In the case of the massless EKG system, the scalar wave modes are only mixed indirectly through their quadratic coupling (via their stress energy tensor) to the gravitational field. As a result, scalar wave modes excite gravitational wave modes at the quadratic order but they excite other scalar modes only at a cubic order. Thus the scalar-scalar interaction is weaker and less interesting physically than the scalar-gravitational interaction. The production of gravitational waves by the scattering of scalar waves has many mathematical features in common with the production of gravitational waves by the motion of fluid bodies. The results presented here demonstrate the versatility of the characteristic code to compute gravitational waves generated by scalar sources and are an encouraging step toward eventually treating a bosonic star in orbit about a black hole.

The massless scalar field coupled minimally with gravitation has been thoroughly studied in 1D. Choptuik [27, 28] carried out the first numerical study of critical behavior in the collapse of massless scalar fields in the context of spherical symmetry. Brady, Chambers and Gonçalves [29] studied critical behavior in the collapse of spherically symmetric massive scalar fields. Seidel and Suen [20] studied the formation of bosonic stars from massive, complex scalar fields. Balakrishna, Seidel and Suen [30] evolved self–gravitating massive scalar fields to study the stability of bosonic star configurations. Recently, axisymmetric simulations of of a complex scalar field have been used to study angular momentum in critical phenomena [31] and fully three dimensional simulations have been used to study bosonic stars [32] and gravitational collapse [33].

A code based upon both incoming and outgoing null cones has been used in a combined global treatment of future infinity and a black hole horizon for an Einstein-Klein-Gordon field with spherical symmetry [7]. Marsa and Choptuik [34] used Eddington–Finkelstein coordinates to study the dispersion of scalar waves in 1D. Siebel, Font and Papadopoulos [35] studied the interaction between a massless scalar field and a neutron star modeled as a perfect fluid. The first characteristic code in Bondi coordinates for the self–gravitating scalar wave problem was constructed by Gómez and Winicour [36]. Subsequently Gómez, Schmidt and Winicour [37] applied the characteristic code to study the radiation tail decay of a scalar field. Barreto *et al.* [38] also used this characteristic code to study the instability of a topological kink in the configuration of the scalar field. Recently, 2-dimensional and 3-dimensional Cauchy simulations of the massless scalar field have been carried out in the perturbative and linearized regimes [39, 40] (and references therein).

The paper is organized as follows. In Sec. II we give the field equations in the characteristic form for a massive, self–interacting, complex scalar field minimally coupled with gravity. In Sec. III we describe the numerical implementation. In Sec. IV we present convergence and stability tests and results for the scattering of a scalar field off a black hole.

II. FIELD EQUATIONS

We use coordinates based upon a family of outgoing null hypersurfaces. We let u label these hypersurfaces; x^A $(A = 2, 3)$ label the null rays and r be a surface area coordinate. In the resulting $x^\alpha = (u, r, x^A)$ coordinates, the metric takes the Bondi–Sachs form [2, 3]

$$ds^2 = -[e^{2\beta}(1 + W/r) - r^2 h_{AB} U^A U^B]du^2 - 2e^{2\beta} dudr \\ -2r^2 h_{AB} U^B du dx^A + r^2 h_{AB} dx^A dx^B, \tag{3}$$

where W is related to the more usual Bondi–Sachs variable V by $V = r + W$, and where $h^{AB} h_{BC} = \delta^A_C$ and $det(h_{AB}) = det(q_{AB})$, with q_{AB} a unit sphere metric. We also use the intermediate variable

$$Q_A = r^2 e^{-2\beta} h_{AB} U^B_{,r}. \tag{4}$$

We work in stereographic coordinates $x^A = (q, p)$ in which the unit sphere metric is

$$q_{AB} dx^A dx^B = \frac{4}{P^2}(dq^2 + dp^2), \tag{5}$$

where

$$P = 1 + p^2 + q^2. \tag{6}$$

We also introduce a complex dyad q_A defined by

$$q^A = \frac{P}{2}(1, i), \tag{7}$$

with $i = \sqrt{-1}$. For an arbitrary Bondi–Sachs metric, h_{AB} can then be represented by its dyad component

$$J = h_{AB} q^A q^B / 2, \tag{8}$$

with the spherically symmetric case given by $J = 0$. The full nonlinear h_{AB} is uniquely determined by J, since the determinant condition implies that the remaining dyad component

$$K = h_{AB} q^A \bar{q}^B / 2 \tag{9}$$

satisfies $1 = K^2 - J\bar{J}$. We also introduce spin–weighted fields

$$U = U^A q_A,\ Q = Q_A q^A, \tag{10}$$

as well as the (complex differential) operators $\eth$ and $\bar{\eth}$ (see [6] for full details).

The null cone problem is normally formulated in the region of space-time between a timelike or null world tube Γ and $\mathcal{I}^+$, with initial data J given on an initial null cone $u = 0$. Boundary data for the metric variables β, Q, U, W and J are required on Γ. We represent $\mathcal{I}^+$ on a finite grid by using a compactified radial coordinate $x = r/(1 + r)$, in terms of which all code variables are globally regular.

The general field equations for a complex scalar field coupled minimally to gravity are

$$R_{ab} = 8\pi(T_{ab} - \frac{1}{2} g_{ab} T), \tag{11}$$

with

$$T_{ab} = \frac{1}{2}(\bar{\phi}_{,a}\phi_{,b} + \phi_{,a}\bar{\phi}_{,b}) - g_{ab}\left(\frac{1}{2} g^{cd}\phi_{,c}\bar{\phi}_{,d} + F\right) \tag{12}$$

where $F(\phi, \bar{\phi})$ includes a possible mass term and self–interacting potential. The scalar field obeys the wave equation

$$\Box\phi - \frac{\partial F}{\partial \bar{\phi}} = 0. \tag{13}$$

In this paper we treat the case of a massless, real scalar field where $F = 0$. The field equations then reduce to

$$R_{ab} = 8\pi\phi_{,a}\phi_{,b}. \tag{14}$$

The corresponding Bondi-Sachs hypersurface equations are

$$\beta_{,r} = 2\pi r(\phi_{,r})^2 + N_\beta, \tag{15}$$

$$(r^2 Q)_{,r} = 16\pi r^2 \phi_{,r}\eth\phi - r^2(\bar{\eth}J + \eth K)_{,r} + 2r^4\eth(\frac{\beta}{r^2})_{,r} + N_Q, \tag{16}$$

$$U_{,r} = \frac{e^{2\beta}}{r^2}(KQ - J\bar{Q}), \tag{17}$$

$$W_{,r} = -2\pi e^{2\beta}[2K\bar{\eth}\phi\eth\phi - J(\bar{\eth}\phi)^2 - \bar{J}(\eth\phi)^2] + \frac{1}{2}e^{2\beta}\mathcal{R} - 1 - e^{\beta}\eth\bar{\eth}e^{\beta} + \frac{1}{4r^2}[r^4(\eth\bar{U} + \bar{\eth}U)]_{,r} + N_W, \tag{18}$$

where

$$\mathcal{R} = 2K - \eth\bar{\eth}K + \frac{1}{2}(\bar{\eth}^2 J + \eth^2\bar{J}) + \frac{1}{4K}(\bar{\eth}\bar{J}\eth J - \bar{\eth}J\eth\bar{J}); \tag{19}$$

and the evolution equation for J is

$$2(rJ)_{,ur} - [V/r(rJ)_{,r}]_{,r} = \frac{8\pi}{r}e^{2\beta}(\eth\phi)^2 - \frac{1}{r}(r^2\eth U)_{,r} + \frac{2}{r}e^{\beta}\eth^2 e^{\beta} - (W/r)_{,r}J + N_J. \tag{20}$$

The expressions for N_β, N_Q, N_W and N_J are given in [10]. The wave equation (13) for the scalar field is

$$2(r\phi)_{,ur} - [V/r(r\phi)_{,r}]_{,r} = -(W/r)_{,r}\phi + N_\phi, \tag{21}$$

where

$$N_\phi = \frac{e^{2\beta}}{r}(N_{\phi 1} - N_{\phi 2} + N_{\phi 3}) - \frac{r}{2}N_{\phi 4} - N_{\phi 5}, \tag{22}$$

$$N_{\phi 1} = K(\eth\bar{\eth}\phi + \eth\beta\bar{\eth}\phi + \bar{\eth}\beta\eth\phi), \tag{23}$$

$$N_{\phi 2} = \frac{1}{2}[\eth\bar{J}\eth\phi + \bar{\eth}J\bar{\eth}\phi + 2(J\bar{\eth}\beta\bar{\eth}\phi + \bar{J}\eth\beta\eth\phi) + J\bar{\eth}^2\phi + \bar{J}\eth^2\phi], \tag{24}$$

$$N_{\phi 3} = \frac{1}{4K}(\bar{J}\bar{\eth}J\eth\phi + J\eth\bar{J}\bar{\eth}\phi + \bar{J}\eth J\bar{\eth}\phi + J\bar{\eth}\bar{J}\eth\phi), \tag{25}$$

$$N_{\phi 4} = \phi_{,r}(\bar{\eth}U + \eth\bar{U}) + 2(U\bar{\eth}\phi_{,r} + \bar{U}\eth\phi_{,r}) + \bar{U}_{,r}\eth\phi + U_{,r}\bar{\eth}\phi, \tag{26}$$

$$N_{\phi 5} = U\bar{\eth}\phi + \bar{U}\eth\phi. \tag{27}$$

The data required on the initial null cone are J and ϕ, which constitute the evolution variables. The remaining auxiliary variables can then be determined on the initial null cone by explicit radial integration in the following order: β from Eq. (15), Q from Eq. (16), U from Eq. (17) and W from Eq. (18). The evolution equations (20) and (21) can then be used to find J and ϕ (in that order) on the "next" null cone. Boundary data on Γ is required for the scalar field ϕ in addition to the gravitational variables J, β, Q, U, and W.

In concluding this section we point out that we obtain the Bondi news function by carrying out a transformation to an inertial frame at $\mathcal{I}^+$. The news is then expressed in terms of the two standard polarization modes N_+ and $N_\times$, as expressed in the computational $\eth$ formalism (for details see Ref.[10]).

III. NUMERICAL IMPLEMENTATION

To solve Eqs. (15)–(21) we follow the strategy developed for the vacuum and fluid matter cases [10, 16] based upon a second–order accurate finite difference approximation. The details follow.

A. Numerical grid

We define a numerical grid with coordinates $(u_n, x_i, q_j, p_k) = (n\Delta u, 1/2+(i-1)\Delta x, -1+(j+3)\Delta q, -1+(k+3)\Delta p)$, where the spatial indexes range from $i = 1 \ldots N_x$, $(j,k) = 1 \ldots N_\zeta$, with $2\Delta x = 1/(N_x-1)$, and $\Delta q = \Delta p = 2/(N_\zeta-5)$. Using finite differences to discretize the equations, we center the derivatives at $(n+1/2, i-1/2, j, k)$. The evolution proceeds with time step Δu, subject to a Courant–Friedrichs–Levy (CFL) condition [9].

B. Hypersurface equations

The hypersurface equations (15)–(18) are discretized as in [10], with the right hand sides now including the scalar field evaluated at the mid-points $x_{i-\frac{1}{2}}$ on the radial grid, which is straightforward to interpolate from the scalar field values at the integral grid points x_i.

C. Evolution equations

The evolution equation (20) for J is treated exactly as in [10] after modifying the right hand side to include the scalar field terms. Thus, we use a Crank–Nicholson scheme to solve the finite difference version of Eq. (20) written in terms of the compactified radial coordinate x. This scheme introduces some numerical dissipation that stabilizes the code even in the regime of very high amplitude fields [10].

We integrate the evolution equation for the scalar field using the null parallelogram marching algorithm [41, 42]. Equation (21) is recast in terms of the 2–dimensional wave operator

$$\Box^{(2)}(r\phi) = e^{-2\beta}[2(r\phi)_{,ru} - (r^{-1}V(r\phi)_{,r})_{,r}] \tag{28}$$

corresponding to the line element

$$d\sigma^2 = 2l_{(\mu}n_{\nu)}dx^\mu dx^\nu = e^{2\beta}[r^{-1}Vdu + 2dr], \tag{29}$$

where $l_\mu = u_{,\mu}$ is the normal to the outgoing null cones and n_μ is an inward normal null vector to the spheres of constant r. The evolution equation for the scalar field then reduces to

$$e^{2\beta}\Box^{(2)}(r\phi) = \mathcal{H}, \tag{30}$$

where

$$\mathcal{H} = -(W/r)_{,r}\phi + N_\phi. \tag{31}$$

Because all 2–dimensional wave operators are conformally flat, with conformal–weight -2, we can apply to (30) a flat–space identity relating the values of $r\phi$ at the corners P, Q, R and S of a null parallelogram $\mathcal{A}$, with sides formed by incoming and outgoing radial characteristics. In terms of $r\phi$, this relation leads to an integral form of the evolution equation for the scalar field:

$$(r\phi)_Q = (r\phi)_P + (r\phi)_S - (r\phi)_R + \frac{1}{2}\int_{\mathcal{A}} dudr\mathcal{H}. \tag{32}$$

The corners of the null parallelogram cannot be chosen to lie exactly on the grid because the velocity of light in terms of x coordinate is not constant. The values of $r\phi$ at the vertices of the parallelogram are approximated to second–order accuracy by linear interpolations between nearest neighbor–grid points on the same outgoing characteristic. Then, by approximating the integrand by its value at the center C of the parallelogram, we have

$$(r\phi)_Q = (r\phi)_P + (r\phi)_S - (r\phi)_R + \frac{1}{2}\Delta u(r_Q - r_P + r_S - r_R)\mathcal{H}_C. \tag{33}$$

In order to apply this scheme globally we must also take into account technical problems concerning the order of accuracy for points near $\mathcal{I}^+$. For this purpose, it is convenient to renormalize (32) by introducing the intermediate variable $\Phi = (r\phi)(1-x) = x\phi$. We choose $\phi = 0$ initially at $\mathcal{I}^+$. The finite difference version of the evolution equation for the scalar field preserves this property. After this substitution, the evolution equation for Φ becomes

$$\Phi_Q = \frac{1}{4}x_Q\Delta u\mathcal{H}_C + \frac{1-x_Q}{1-x_P}\left(\Phi_P + \frac{1}{4}x_P\Delta u\mathcal{H}_C\right) + \frac{1-x_Q}{1-x_S}\left(\Phi_S + \frac{1}{4}x_S\Delta u\mathcal{H}_C\right) - \frac{1-x_Q}{1-x_R}\left(\Phi_R + \frac{1}{4}x_R\Delta u\mathcal{H}_C\right). \quad (34)$$

Since Φ_Q is defined by linear interpolation, we find (for $2 < i < N_x$)

$$\phi_i^{n+1} = \frac{\Phi_Q\Delta x - \Phi_{i-1}^{n+1}(x_i - x_Q)}{x_i(x_Q - x_{i-1})}; \quad (35)$$

and for $i = 2$ or $i = N_x$,

$$\phi_i^{n+1} = \frac{\Phi_Q}{x_i}. \quad (36)$$

IV. SCATTERING OF A MASSLESS SCALAR FIELD OFF A SCHWARZSCHILD BLACK HOLE

A. Setting the initial and boundary data

We use the code to evolve an initial configuration where the gravitational data corresponds to a Schwarzschild black hole of mass $M = 1$ superimposed with initial data of compact radial support for the massless scalar field. The initial gravitational data are

$$J(u = 0, x, x^A) = 0. \quad (37)$$

In the absence of the scalar field, these data would generate the Schwarzschild solution throughout the exterior Kruskal quadrant. In the presence of the scalar field, the inner Schwarzschild white hole horizon is undisturbed but the black hole horizon is dynamically deformed. Note that there are no elliptic constraints in prescribing characteristic gravitational data, as opposed to the corresponding Cauchy problem.

The data at the inner boundary Γ, located at $r = 2M$, are

$$\beta = 0,\ Q = 0,\ U = 0,\ W = -2M,\ J = 0,\ \phi = 0. \quad (38)$$

We take as the initial data for the scalar field

$$r\phi(u = 0, r, q, p) = \begin{cases} \lambda(r - r_a)^4(r - r_b)^4 G(q, p) & \text{if } r \in [R_a, R_b], \\ 0 & \text{otherwise.} \end{cases} \quad (39)$$

Such data, prescribed here on an outgoing null hypersurface, corresponds to an ingoing pulse of scalar radiation. For $G(q, p) = 1$, the pulse would be a spherically symmetric shell with amplitude λ located between r_a and r_b. For the convergence test in this paper, in both hemispheres we take G to be the function

$$G(q, p) = \begin{cases} [R_s^2 - \mu]^4 & \text{if } R_s^2 \le \mu, \\ 0 & \text{otherwise,} \end{cases} \quad (40)$$

where $R_s^2 = (q - q_s)^2 + (p - p_s)^2$. Axisymmetric and non-axisymmetric initial massless scalar field configurations can be obtained depending on the values of q_s, p_s and μ. For $q_s = p_s = 0$, the initial profile of $r\phi$ is axisymmetric about the poles and goes to zero at $q^2 + p^2 = \mu$. For other values of (q_s, p_s), ϕ is in general asymmetric.

B. Monitoring convergence

We measure convergence of the scalar field in terms of the norm

$$\mathcal{Q}(u) = 4\int\left(\frac{\phi}{P}\right)^2 dqdpdx, \quad (41)$$

where the integration volume is taken over the entire null hypersurface exterior to $r = 2M$. We use the four–point formula

$$\mathcal{Q} = \sum_{j,k} (\phi^2_{j,k} + \phi^2_{j\pm1,k} + \phi^2_{j,k\pm1} + \phi^2_{j\pm1,k\pm1}) \frac{dq\,dp}{P^2_{j\pm\frac{1}{2},k\pm\frac{1}{2}}}, \tag{42}$$

for the contribution from cells contained completely in the upper and lower hemisphere. For a cell that crosses the equator, we approximate the equator by a straight line and evaluate the cell's additional contribution to (42) by

$$\mathcal{Q} = \ldots + \left[\left(\frac{\phi}{P}\right)^2_{j,k} + \left(\frac{\phi}{P}\right)^2_{j\pm1,k} + \left(\frac{\phi}{P}\right)^2_{j,k\pm1} + \left(\frac{\phi}{P}\right)^2_{j\pm1,k\pm1} \right] dS_{j,k}, \tag{43}$$

where $dS_{j,k}$ is the trapezoidal surface element. The integration in x is straightforward; we use a second–order accurate Simpson's formula. The computation of (41) is the same order of finite difference approximation as used to solve (15)–(18).

For the convergence test we take $r_a = 3.5$ and $r_b = 12$, $\lambda = 10^{-7}$, $\mu = 0.3$ and $q_s = p_s = 0$. This gives an axisymmetric, equatorial reflection symmetric configuration corresponding to two ingoing pulses centered about the axis of symmetry. The following grids were used:

- Coarse, $n_x = 41$, $n_q = n_p = 25$
- Medium, $n_x = 81$, $n_q = n_p = 45$
- Fine, $n_x = 161$, $n_q = n_p = 85$,

for which Δx and $\Delta q = \Delta p$ scale as $4 : 2 : 1$. Assuming that the quantity $\mathcal{Q}$ behaves as $\mathcal{Q} = a + b\Delta^n$, it can be shown that the convergence rate is

$$n = \log_2 \frac{\mathcal{Q}_c - \mathcal{Q}_m}{\mathcal{Q}_m - \mathcal{Q}_f}, \tag{44}$$

where $\mathcal{Q}_c$, $\mathcal{Q}_m$ and $\mathcal{Q}_f$ refer to computed values of $\mathcal{Q}$ using the coarse, medium and fine grids, respectively [17]. The results in Table I show that the 3-dimensional EKG code is second order convergent in amplitude.

We also measure the convergence in phase. It can be easily shown that the order of convergence in phase is expressed by

$$n = \log_2 \frac{\mathcal{Q}_{cm}}{\mathcal{Q}_{mf}}, \tag{45}$$

where

$$\mathcal{Q}_{cm} = 4 \int \left[\frac{(\phi_c - \phi_m)}{P} \right]^2 dqdpdx$$

and

$$\mathcal{Q}_{mf} = 4 \int \left[\frac{(\phi_m - \phi_f)}{P} \right]^2 dqdpdx$$

are calculated at the same grid points and at the same time by sub-sampling from the fine and medium grids to the coarse one. The results in Table II confirm that our code is also second order convergent in phase.

C. Verifying the stability of the EKG-PITT code

We have tested the code by carrying out numerical experiments which confirm that it is stable, subject to the CFL condition. The stability test consists of evolving random, initially localized scalar data of small amplitude for a sufficiently long time. The data is chosen to be random so that all possible numerical frequencies at a given resolution are present. Hence, any unstable mode is most likely to be excited and to dominate the evolution in the number of time steps taken. In particular, data of amplitude $|\phi| \simeq 10^{-8}$ was run from $u = 0$ to $u = 50$, corresponding to 2×10^4 time steps for the coarse grid and 4×10^4 time steps for the medium grid. During this time, the norm $\mathcal{Q}(u)$ initially decreases due to scattering of the scalar field. Figure 1 shows that the norm remains bounded at the end of the run, with a value of $\mathcal{Q} \approx 6 \times 10^{-17}$.

D. Scattering, scaling and mode coupling of axisymmetric pulses off a black hole

We first consider initial data (39) describing an $\ell = 2$, $m = 0$ massless scalar pulse propagating inward toward a Schwarzschild black hole, with the boundary conditions (38) and initial gravitational data (37). The parameters of the initial data are $r_a = 3$, $r_b = 5$, $\lambda = 10^{-8}$. The radial location of the initial pulse is chosen for computational economy since nonlinear effects are weak for $r >> 3M$. Figure 2 shows the computed time dependence of $r\phi$ at $\mathcal{I}^+$, overlaid with the analytic curve for the corresponding quasi-normal mode calculated from perturbation theory [43, 44]. After $u = 10M$, the ringdown of the computed waveform agrees with the complex frequency $\bar{\omega} = 0.4875 - i0.098$, obtained in the perturbative treatment of a scalar field on a Schwarzschild background.

Next we consider the scattering of an $\ell = 1$, $m = 0$ scalar pulse, with $r_a = 3$, $r_b = 5$, for a range of amplitudes λ. Figure 3 show the rescaled scalar waveform $r\phi/\lambda$ scattered to $\mathcal{I}^+$ in the $q = p = 0$ direction; and Fig. 4 shows the rescaled component N_+/λ^2 of the gravitational news function at $\mathcal{I}^+$ in the $q = p = 0.5$ direction. All the curves overlap for $\lambda = 10^{-5}, 10^{-4}, 10^{-3}$. Thus it is manifest that $r\phi$ has a linear dependence on amplitude and N_+ has a quadratic dependence, as expected. The results also show that $\ell = 1$ is the lowest scalar mode that generates gravitational radiation. The quasinormal frequency calculated using perturbation theory is $\bar{\omega} = 0.292935 - i0.09766$ [43, 44]. A comparison of the numerical and perturbative scalar waveforms over the time interval $u < 20$ reveals good agreement between the oscillation periods. However, during this time interval the numerical waveform does not yet display a clean quasinormal decay. Further investigation of this feature would require longer runs with higher resolution.

Now we consider scattering of an axisymmetric scalar "blob" (39) of compact support $q^2 + p^2 \leq 0.4$ on the north patch, with $r_a = 3$, $r_b = 5$, $\lambda = 10^{-1}$ and

$$G(q, p) = \left[\frac{q^2 + p^2 - 0.4}{q^2 + p^2 + 1}\right]^4 . \tag{46}$$

The initial angular structure is dominated by the $\ell = 1$, $m = 0$ harmonic. Figures 5 and 6 display snapshots of the evolution of $r\phi$ and the spin-weight invariant $J\bar{J}$ at $\mathcal{I}^+$, respectively, on the North hemisphere, obtained with a resolution of 89×89 angular grid points and 101 radial grid points. The radiation pattern has sharp angular features arising from the phase differences between the backscattering at different angles. The angular resolution is sufficient to reveal the main features of the evolution in fairly smooth snapshots. The numerical evolution of the axisymmetric initial data preserves the axisymmetry. The gravitational invariant $J\bar{J}$ vanishes at the pole $q = p = 0$, as required by axisymmetry. Figure 7 shows a global view of how the scalar field is backscattered to infinity while approaching the black hole.

Figures 8 and 9 display the rescaled radiation amplitudes $r\phi/\lambda$ and N_+/λ^2 at $\mathcal{I}^+$ produced on the North hemisphere by the scattering of the blob with varying amplitude λ. Once again, the scalar field radiation pattern scales linearly and the gravitational polarization mode N_+ scales quadratically for incident amplitudes up to $\lambda = 10^{-1}$. Note in Fig. 9 that the scaling of N_+ breaks down at the very small $\lambda = 10^{-12}$ amplitude where the quadratic response is below numerical error.

It is also possible to analyze the nonlinear content of the scalar waveform at $\mathcal{I}^+$ by decomposing it in the spin-0 spherical harmonic amplitudes

$$F_{lm} = \oint r\phi Y_{lm} d\Omega. \tag{47}$$

These are computed by second order accurate integration over the sphere (with solid angle $\Omega = 4\pi$). We vary the amplitude of the ingoing axisymmetric blob from $\lambda = 10^{-12}$ to $\lambda = 10^{-1}$ and carry out the simulations with a resolution of 25×25 angular grid points and 41 radial grid points (the coarse grid in the convergence tests). This is sufficient to illustrate the qualitative behavior with reasonable computational expense. We display the results for $F_{lm}(u)/\lambda$, with $l = 2$, 4, 6 and $m = 0$, in Figs. 10–12.

The graph of $F_{20}(u)/\lambda$ in Fig. 10 shows that the radiation amplitude varies linearly with input amplitude λ, even at the larger amplitudes. The graphs in Fig's 11 and 12 of $F_{40}(u)/\lambda$ and $F_{60}(u)/\lambda$ show similar behavior, i.e. a predominantly linear response, without nonlinear effects on the scalar field radiation. Thus it appears that up to an amplitude of $\lambda = 10^{-1}$ that the scattered waveform of the scalar field is in excellent agreement with results obtained by perturbation theory on a Schwarzschild background. This is in accord with expectations since the nonlinear effects are introduced by the gravitational field and thus are $O(\lambda^3)$ compared with the $O(\lambda)$ linear terms.

E. Scattering of a non-axisymmetric pulse off a black hole

In order to confirm the robustness of the implementation, we consider the scattering of an *asymmetric* scalar blob of compact support by a Schwarzschild black hole. The initial pulse (39) has parameters $\lambda = 10^{-7}$, $r_a = 3.5$, $r_b = 12$,

$\mu = 0.03$, with offset $q_s = 0.2$, $p_s = 0.3$ (which breaks the axisymmetry). The evolution is carried out on a $85 \times 85 \times 101$ grid.

Figures 13 and 14 show surface plots at $\mathcal{I}^+$, at four different times, of the resulting scalar radiation $r\phi$ and the gravitational wave energy flux $|N|^2 = |N_+|^2 + |N_\times|^2$, respectively. As the evolution proceeds, the nonlinear effects produce a rich structure in the gravitational radiation. It is also clear from the snapshots of the scalar field that much finer angular grids are necessary to obtain smooth results in the asymmetric case.

F. Speed of the code

The tests were performed on Linux machines with a single AMD Athlon T-Bird processor running at $900MHz$. One unit of physical time on a grid of $85 \times 85 \times 101$ points takes about 21 hours.

V. CONCLUSION

In this paper we have incorporated a massless scalar field into a 3-dimensional characteristic code for the Einstein field equations. The code has been verified to be stable and convergent. A scalar field provides a clean way to simulate a variety of physically interesting scenarios:

- Highly-perturbed black holes. The single black hole formed just after the merger of a binary black hole, or just after the asymmetric collapse of a star, would be highly distorted. A fully nonlinear general relativistic code is necessary to probe this regime. This requires a stable code that can deal with a single, dynamical, black hole and a "perturbing" agent, as can be modeled by a scalar field. Recent studies of gravitational waves incident on a black hole [24] have revealed interesting phenomena arising from such highly nonlinear perturbations of the gravitational field. The scalar field provides an alternative perturbation to shed light on the robustness of these effects.

- Toroidal distributions of "sources" around black holes. Toroidal distributions of matter fields around black holes play a major role in models describing active galactic nuclei, quasars and even gravitational wave sources. A successful simulation of these systems will require, at the very least, robust general relativistic codes appropriately coupled to relativistic hydrodynamics. A toroidal scalar field distribution around a black hole represents a intermediate step for assessing the performance of the implementation. Although this has limitations, it does provide a geometrical set up similar to the one expected in real astrophysical sources. Therefore, it can shed light on issues such as the gravitational wave output of physical systems, the characteristics of the expected waveforms, the radiated angular momentum, etc. Additionally, the equivalence of a massless scalar field to an irrotational stiff fluid provides a simple computational alternative to general relativistic hydrodynamics [45], which can be used to probe the interaction of the torus with the black hole. Preliminary relativistic hydrodynamical simulations already reveal that this system gives rise to rich scenarios [46, 47].

- Stability of Kerr black holes under massive scalar fields. Although the stability question of Schwarzschild black holes has been settled [48], the problem for spinning black holes is still quite open. In particular, it has been pointed out that for massive scalar fields, unstable modes are likely [49, 50]. A mathematical analysis of such a system is complicated even in the axisymmetric case [51]. Numerical simulations of massive scalar perturbations might help shed light on this problem.

- Boson star orbiting a black hole [19, 20]. Such a simulation would shed light on both the orbital decay and the waveform radiated to null infinity. While this is perhaps the physically most interesting project, it is also the most computationally demanding because of the necessity to resolve the compact distribution of the scalar field.

Some of the above projects can already be studied with the code as implemented in this work. However, for more "realistic" scenarios one would like to extend this treatment to include massive scalar fields and spinning black holes. Work in these directions is in progress.

Acknowledgments

We thank M. Choptuik, J. Pullin and Y. Zlochower for their input. For correspondence on the quasinormal frequencies of scalar radiation we also wish to thank H. Beyer, L. Burko, K. Kokkotas and R. Price; Price also directed

us to reference [44]. This work was supported by FONACIT under grant S1–98003270, the National Science Foundation under grants PHY-0244673 to the University of Pittsburgh and PHY-0135390 to Carnegie Mellon University and PHY-0244673 to Louisiana State University and NASA under NASA-NAG5-1430 to Louisiana State University. Computer time was provided by the Centro Nacional de Cálculo Científico de la Universidad de los Andes (CeCalcULA).

---

[1] J. York, "Kinematics and dynamics of general relativity", in *Sources of Gravitational Radiation*, 83–126, Ed. L. L. Smarr, Cambridge University Press, Cambridge (1979).
[2] H. Bondi, M. G. Van der Burg and A. W. Metzner, Proc. R. Soc. London Ser. A **269**, 21 (1962).
[3] R. K. Sachs, Proc. R. Soc. London Ser. A, **270**, 103 (1962).
[4] R. Penrose, Phys. Rev. Lett. **10**, 66 (1963).
[5] R. A. Isaacson, J. S. Welling and J. Winicour, J. Math. Phys. **24**, 1824 (1983).
[6] R. Gómez, L. Lehner, P. Papadopoulos and J. Winicour, Class. Quantum Grav. **14**, 4, 977 (1997), gr-qc/9702002.
[7] L. Lehner, Int. J. Mod. Phys. D **9**, 459 (2000), gr–qc/9911033.
[8] R. Gómez, Phys. Rev. D **64**, 024007 (2001), gr–qc/0103011.
[9] N. T. Bishop, R. Gómez, L. Lehner and J. Winicour, Phys. Rev. D **54** 6153 (1996), gr–qc/9705033.
[10] N. T. Bishop, R. Gómez, L. Lehner, M. Maharaj and J. Winicour, Phys. Rev. D **56**, 10, 6298 (1997), gr–qc/9708065.
[11] R. Gómez, L. Lehner, R. L. Marsa and J. Winicour, Phys. Rev. D **57**, 8, 4778 (1998), gr–qc/9710138.
[12] R. Gómez, R. L. Marsa and J. Winicour, Phys. Rev. D **56**, 10, 6310 (1997), gr–qc/9708002.
[13] E. T. Newman and R. Penrose, J. Math. Phys. **7**, 863, (1966).
[14] Y. Zlochower, Ph. D. dissertation, University of Pittsburgh (2002).
[15] N. T. Bishop and S. S. Deshingkar, Phys. Rev. D **68**, 024031 (2003), gr–qc/0303021.
[16] N. T. Bishop, R. Gómez, L. Lehner, M. Maharaj and J. Winicour, Phys. Rev. D **60**, 2, 24005 (1999), gr–qc/9901056.
[17] N. T. Bishop, R. Gómez, S. Husa, L. Lehner and J. Winicour, Phys. Rev. D **68**, 084015 (2003), gr–qc/0301060.
[18] J. R. Primack, D. Seckel and B. Sadoulet, Ann. Rev. Nucl. Part. Sci. **38**, 751, (1988).
[19] E. Seidel and W-M. Suen, Phys. Rev. Lett. **66**, 1659 (1991).
[20] E. Seidel and W-M. Suen, Phys. Rev. Lett. **72**, 2516 (1994), gr–qc/9309015.
[21] T. D. Lee and Y. Pang, Phys. Rep. **221**, 251, (1992).
[22] P. Jetzern, Phys. Rep. **220**, 183, (1992).
[23] A. R. Liddle and M. S. Madsen, Int. J. Mod. Phys. D **1**, 101, (1992).
[24] Y. Zlochower, R. Gómez, S. Husa, L. Lehner and J. Winicour, Phys. Rev. D **68**, 084014 (2003), gr–qc/0306098.
[25] G. Allen, K.Camarda and E. Seidel, *Evolution of Distorted Black Holes: A Perturbative Approach*, gr–qc/9806014.
[26] J. Baker, S. Brandt, M. Campanelli, C. O. Lousto, E. Seidel, and R. Takahashi, Phys. Rev. D **62**, 127701 (2000), gr–qc/9911017.
[27] M. W. Choptuik, Phys. Rev. Lett. **70**, 1, 9 (1993).
[28] C. Gundlach, "Critical Phenomena in Gravitational Collapse", Living Rev. Relativity **2**, 4 (1999), http://www.livingreviews.org/lrr-1999-4.
[29] P. R. Brady, C. M. Chambers and S. M. C. V. Goncalves, Phys. Rev. D **56**, R6057 (1997), gr–qc/9709014.
[30] J. Balakrishna, E. Seidel and W. M. Suen, Phys. Rev. D **58**, 104004 (1998), gr–qc/9712064.
[31] M. W. Choptuik, E. W. Hirschmann, S. L. Liebling and F. Pretorius, Phys. Rev. Lett. **93**, 131101 (2004).
[32] F. S. Guzman, Phys. Rev. D **70**, 044033 (2004)
[33] F. Pretorius, arXiv:gr-qc/0407110.
[34] R. L. Marsa and M. W. Choptuik, Phys. Rev. D **54**, 4929 (1996), gr–qc/9607034.
[35] F. Siebel, J. A. Font and P. Papadopoulos, Phys. Rev. D **65**, 024021 (2002), gr–qc/0108006.
[36] R. Gómez and J. Winicour, J. Math. Phys. **33**, 4, 1445 (1992).
[37] R. Gómez, J. Winicour and B. G. Schmidt, Phys. Rev. D **49**, 6, 2828 (1994).
[38] W. Barreto, R. Gómez, L. Lehner and J. Winicour, Phys. Rev. D **54**, 6, 3834 (1996).
[39] M. A. Scheel, A. L. Erickcek, L. M. Burko, L. E. Kidder, H. P. Pfeiffer and S. A. Teukolsky, Phys. Rev. D **69**, 104006 (2004), gr–qc/0305027.
[40] M. W. Choptuik, E. W. Hirschmann, S. L. Liebling and F. Pretorius, Phys. Rev. D **68**, 044007 (2003), gr–qc/0305003.
[41] R. Gómez, P. Papadopoulos and J. Winicour, J. Math. Phys. **35**, 8, 4184 (1994), gr–qc/0006081.
[42] J. Winicour, "Characteristic Evolution and Matching", Living Rev. Relativity **4**, 3 (2001), http://www.livingreviews.org/lrr-2001-3.
[43] K. Kokkotas and H. Beyer, Private communication (2004).
[44] R. Konoplya, Journal of Physical Studies, **8** N1, 93 (2004).
[45] P. Brady, M. Choptuik, C. Gundlach and D. Neilsen, Class. Quantum Grav. **19**, 6359 (2002), gr–qc/0207096.
[46] S. L. Shapiro, arXiv:astro-ph/0404338.
[47] O. Zanotti, J. A. Font, L. Rezzolla and P. J. Montero, arXiv:astro-ph/0411116.
[48] B. S. Kay and R. M. Wald, Class. Quantum Grav. **4**, 893 (1987).
[49] S. Detweiler, Phys. Rev. D **22**, 2323 (1980).
[50] R. Damour, N. Deruelle and R. Ruffini, Lett. Nuovo Cimento **15**, 257 (1976).

[51] H. R. Beyer, Commun. Math. Phys. **221**, 659 (2001), astro–ph/0008236.

TABLE I: Convergence in amplitude of the 3-dimensional EKG code

u	$\mathcal{Q}_c$ (10^{-12})	$\mathcal{Q}_m(10^{-12})$	$\mathcal{Q}_f(10^{-12})$	n
0.05	3.718	3.742	3.748	1.99
0.10	3.684	3.708	3.713	1.99
0.15	3.653	3.675	3.681	1.99
0.20	3.623	3.645	3.651	1.99

TABLE II: Convergence in phase of the 3-dimensional EKG code

u	$\mathcal{Q}_{cm}$ (10^{-14})	$\mathcal{Q}_{mf}(10^{-15})$	n
0.05	2.465	6.270	1.97
0.10	2.429	6.204	1.97
0.15	2.404	6.141	1.97
0.20	2.382	6.083	1.97

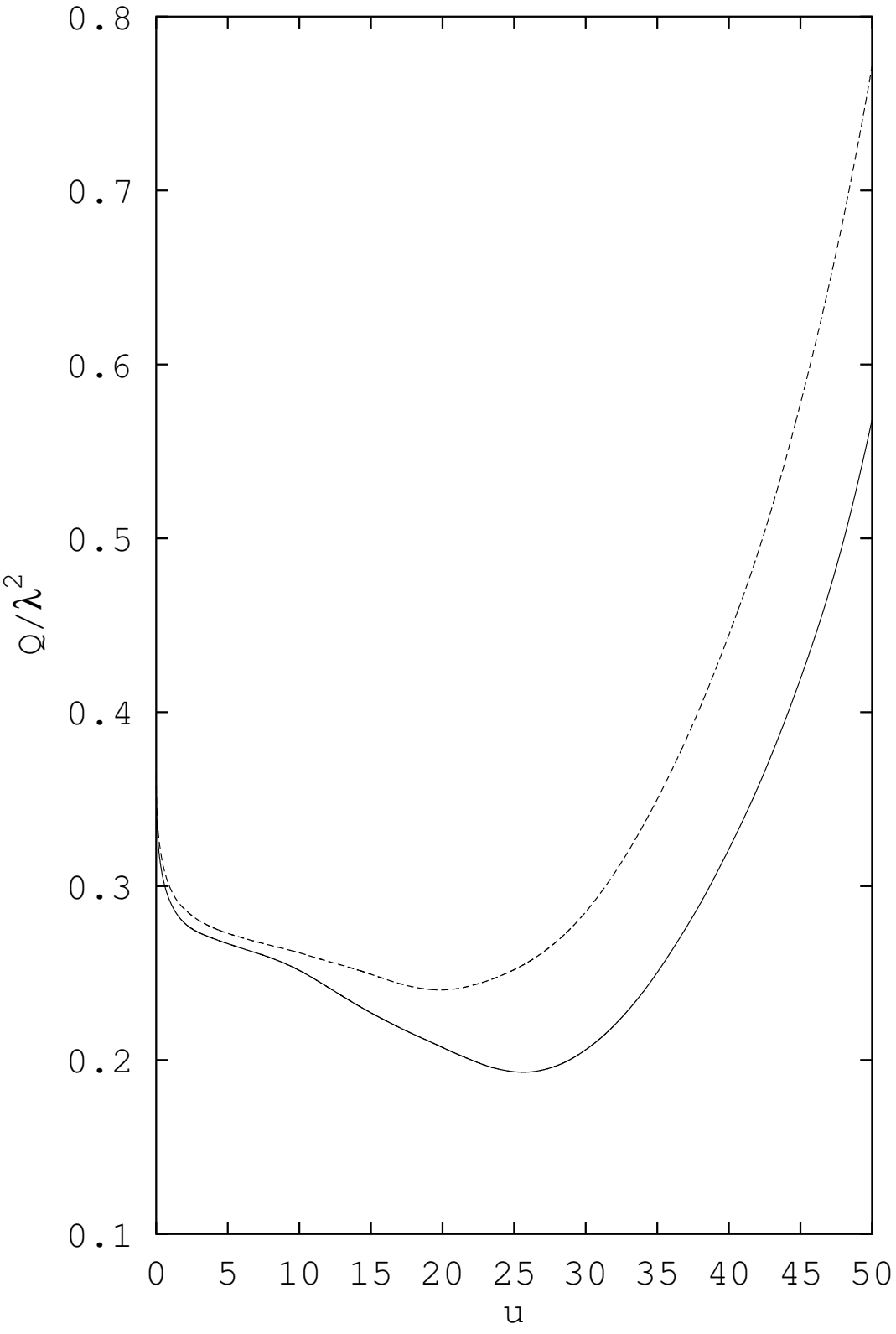

FIG. 1: The scalar field norm $\mathcal{Q}/\lambda^2$ is plotted *vs* retarded time u for random initial scalar data with amplitude $\lambda = 10^{-8}$ in a localized region between $r_a = 3$ and $r_b = 5$ on a grid of size $n_x = 41$, $n_q = n_p = 25$. The dashed line plots the rescaled norm $\mathcal{Q}/\lambda^2$ for the same initial random data but with $\lambda = 2.5 \times 10^{-9}$ on a grid of size $n_x = 81$, $n_q = n_p = 45$.

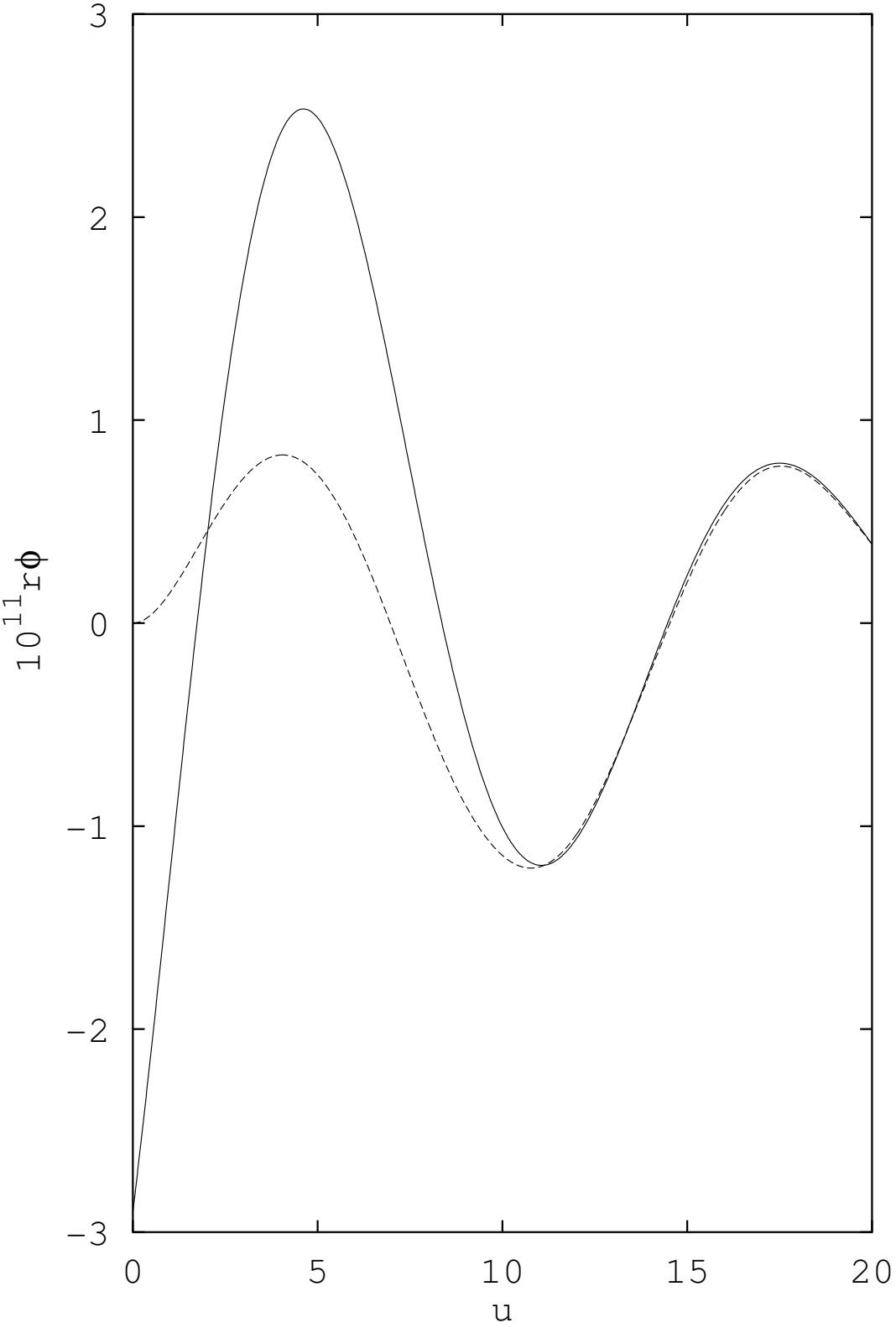

FIG. 2: The dashed line plots the waveform $r\phi(u)$ (multiplied by 10^{11}) radiated to $\mathcal{I}^+$ in the $q = p = 0$ direction resulting from the backscattering of an $l = 2$, $m = 0$ pulse. The pulse parameters for the initial data are $r_a = 3$; $r_b = 5$, $\lambda = 10^{-8}$. The grid size is $25 \times 25 \times 101$. The solid line is the analytic curve corresponding to the complex quasi-normal mode frequency $\bar{\omega} = 0.4875 - i0.098$ obtained from a perturbation calculation.

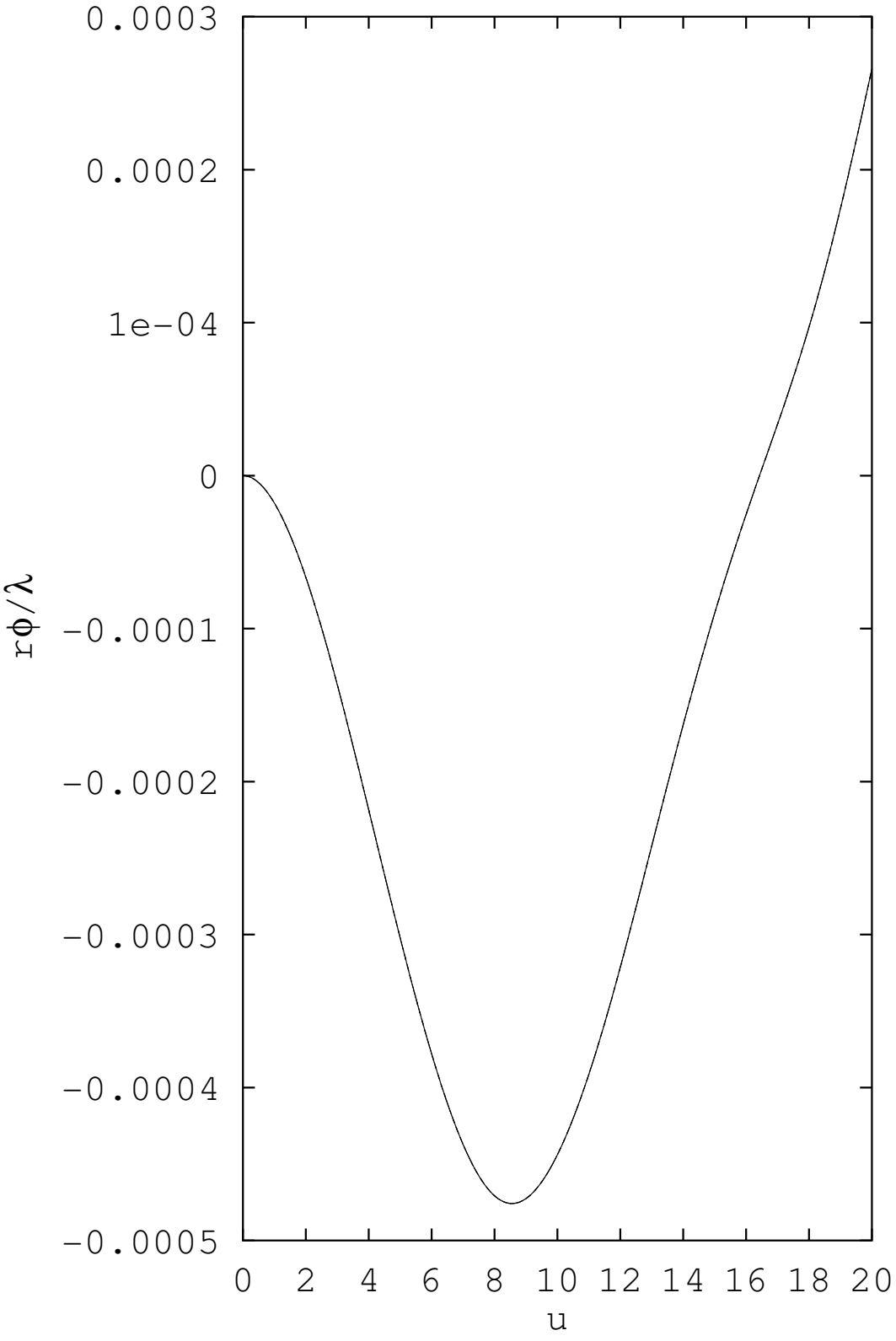

FIG. 3: The rescaled waveform $r\phi(u)/\lambda$ is plotted for the $q = p = 0$ direction at $\mathcal{I}^+$. The parameters of the initial data are: $r_a = 3$; $r_b = 5$, $\ell = 1$, $m = 0$. The grid size is $25 \times 25 \times 101$. All the curves overlap for $\lambda = 10^{-5}, 10^{-4}, 10^{-3}$.

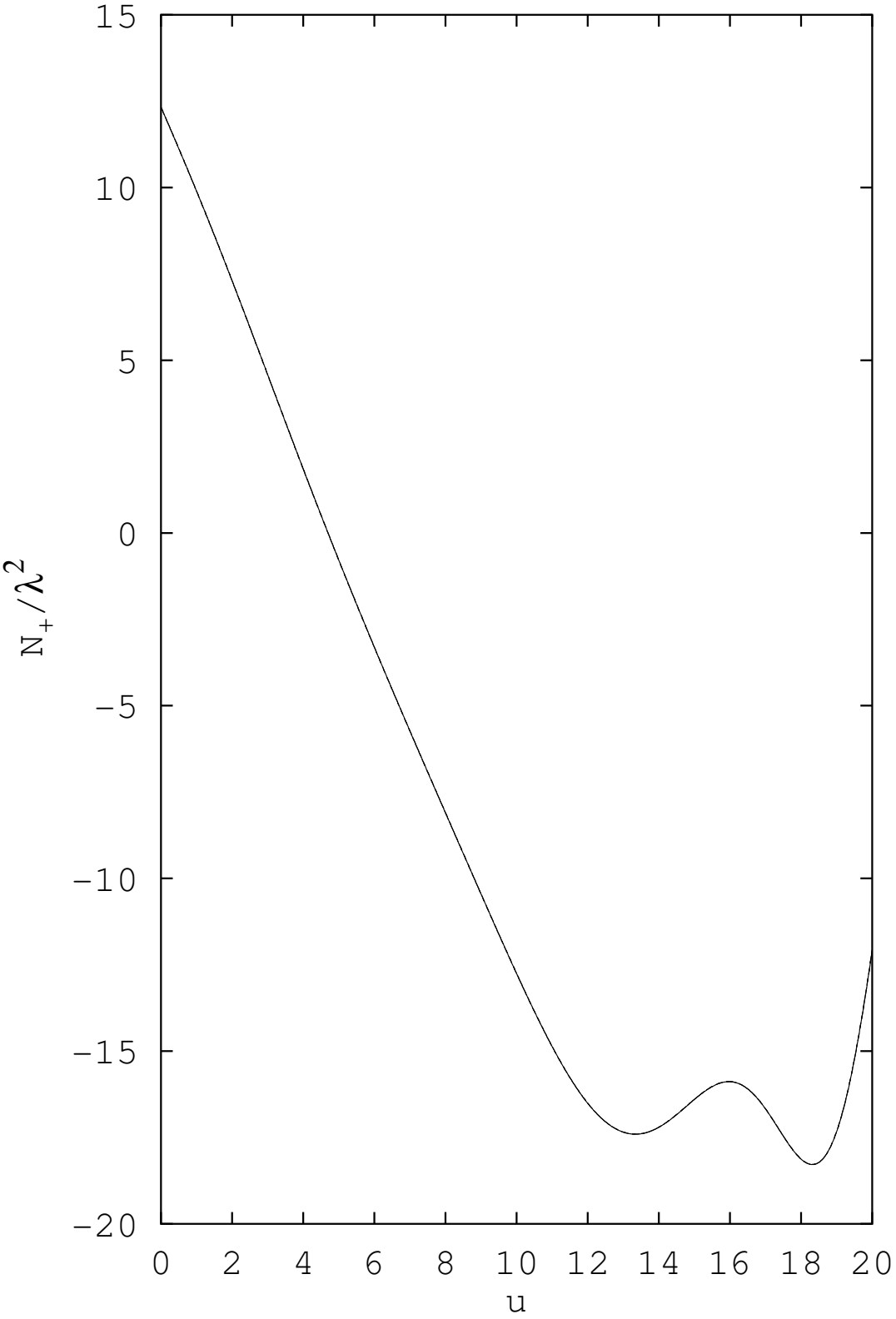

FIG. 4: The rescaled news function component $N_+(u)/\lambda^2$ is plotted for the $q = p = 0.5$ direction at $\mathcal{I}^+$. The initial data parameters are $r_a = 3$; $r_b = 5$, $\ell = 1$, $m = 0$. The grid size is $25 \times 25 \times 101$. All the curves overlap for $\lambda = 10^{-5}, 10^{-4}, 10^{-3}$.

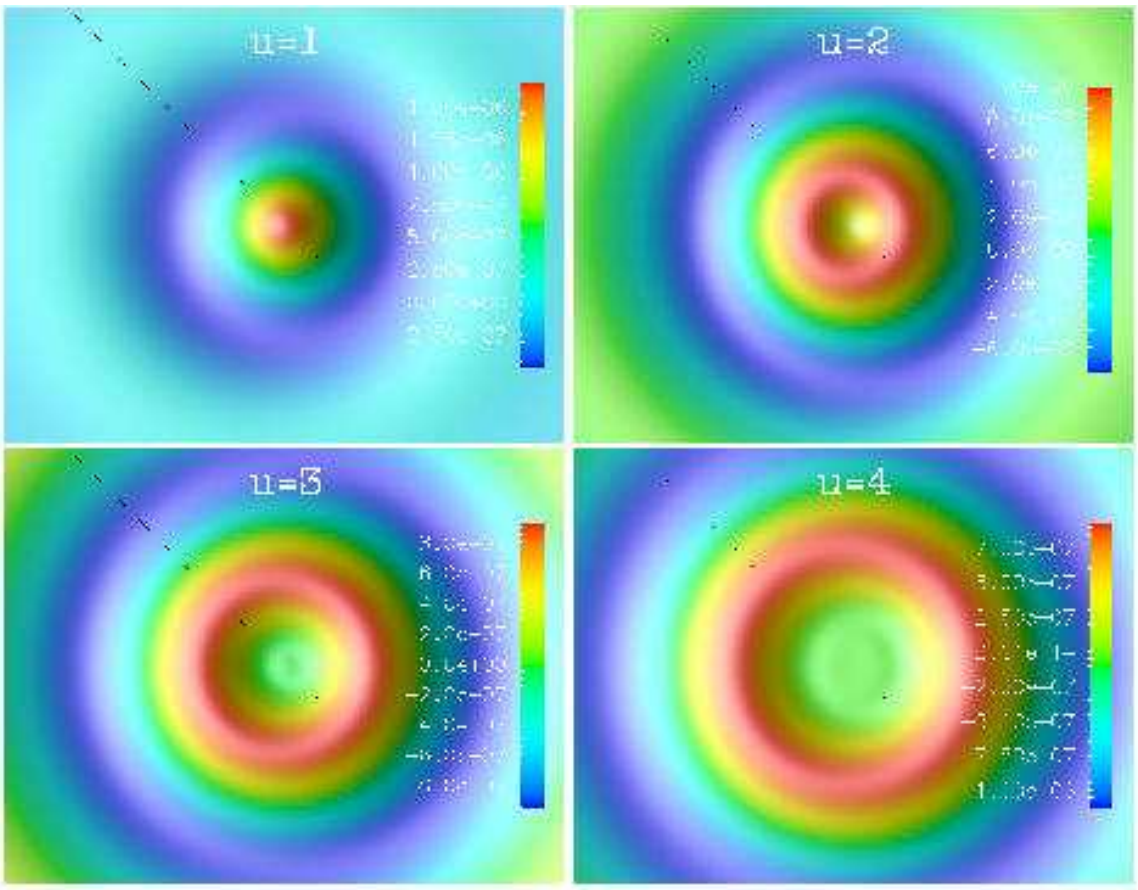

FIG. 5: Axisymmetric surface plots of $r\phi$ on the North patch of $\mathcal{I}^+$ for $u = 1, 2, 3, 4$, in zig–zag order from top to bottom, resulting from the scattering of an axisymmetric pulse. The parameters of the initial data are $r_a = 3$ $r_b = 5$ $\lambda = 10^{-1}$. The grid size is $89 \times 89 \times 101$.

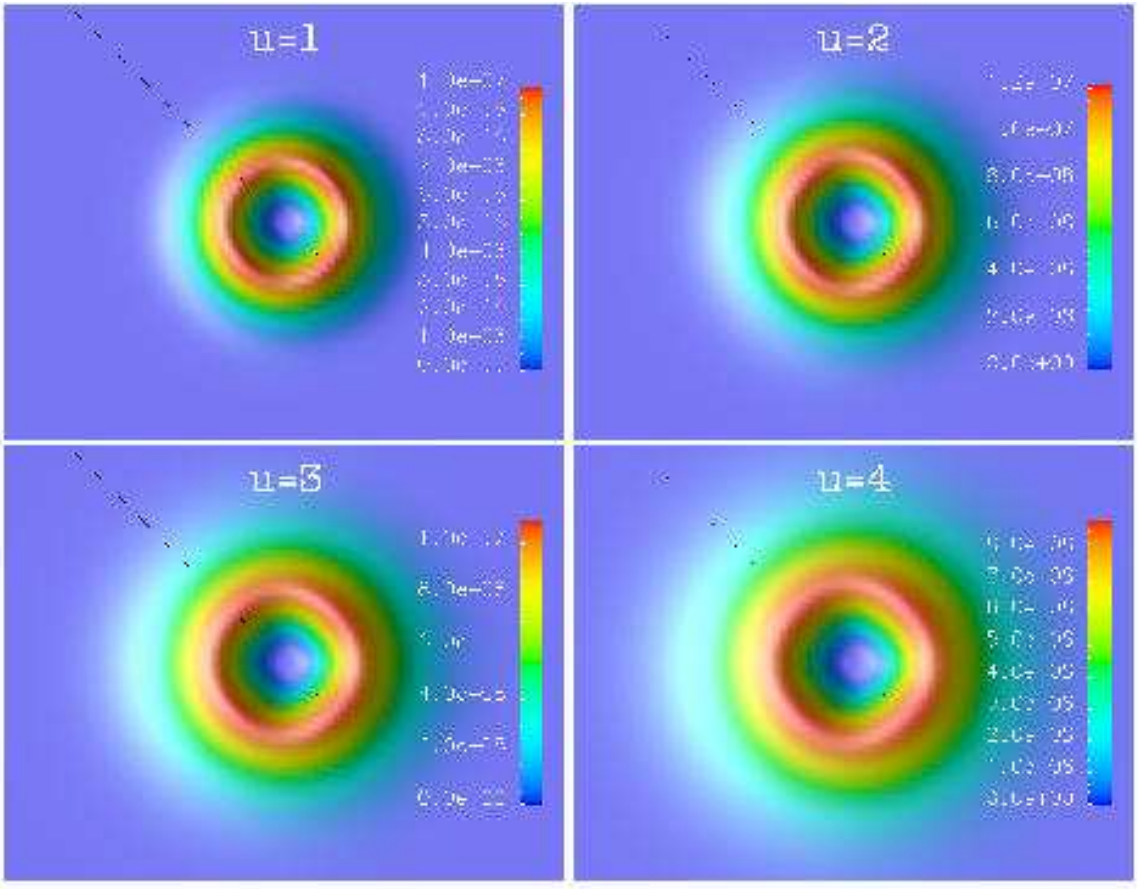

FIG. 6: Surface plots of the spin-weight invariant $J\bar{J}$ on the North patch of $\mathcal{I}^+$ for $u = 1, 2, 3, 4$, in zig–zag order from top to bottom, resulting from the scattering of an axisymmetric pulse with initial data parameters $r_a = 3$, $r_b = 5$, $\lambda = 10^{-1}$. The grid size is $89 \times 89 \times 101$.

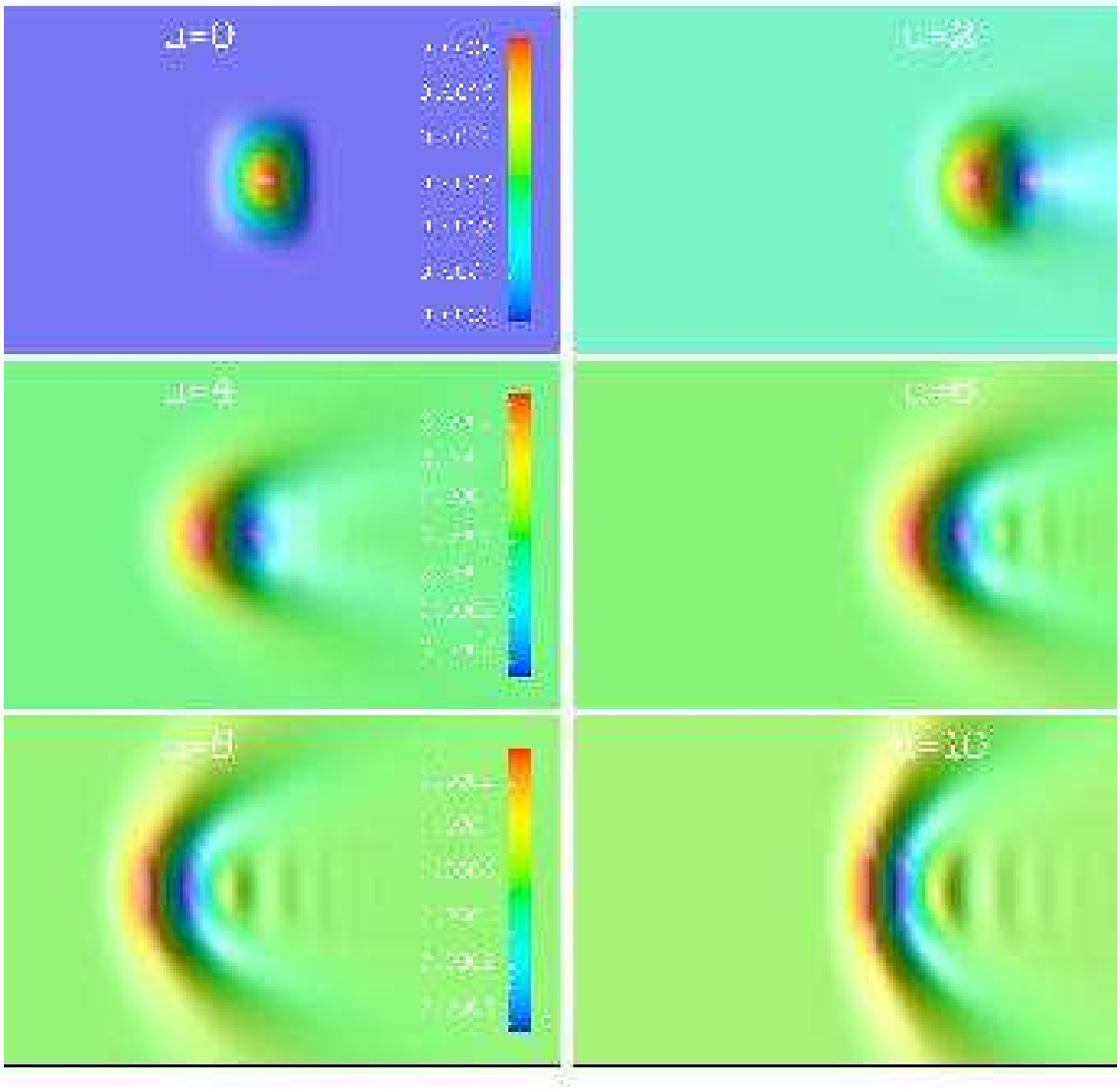

FIG. 7: Global radial-angular view of $r\phi$ on the North patch for $u = 0, 2, 4, 6, 8, 10$, in zig–zag order from top to bottom. We set $p = 0$, $-1.2 < q < 1.2$ (from bottom to top), $0.5 < x < 1.0$ (from left to right). The initial data parameters are $r_a = 3$, $r_b = 5$, $\lambda = 10^{-1}$. The grid size is $25 \times 25 \times 41$.

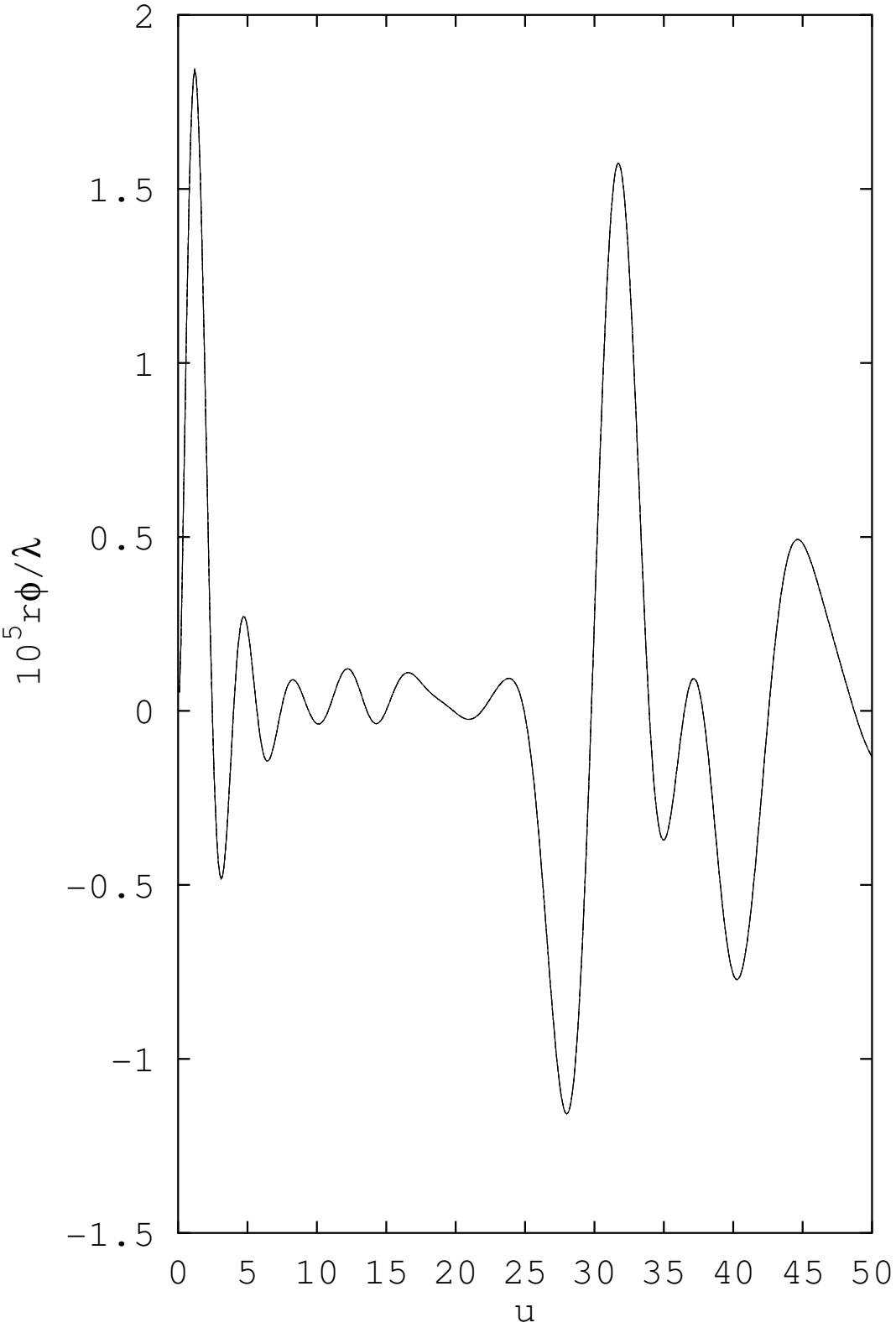

FIG. 8: $r\phi(u)/\lambda$ (multiplied by 10^5) is plotted for the $q = p = 0$ direction at $\mathcal{I}^+$; all the curves overlap for $\lambda = 10^{-12}, 10^{-3}, 10^{-2}, 10^{-1}$.

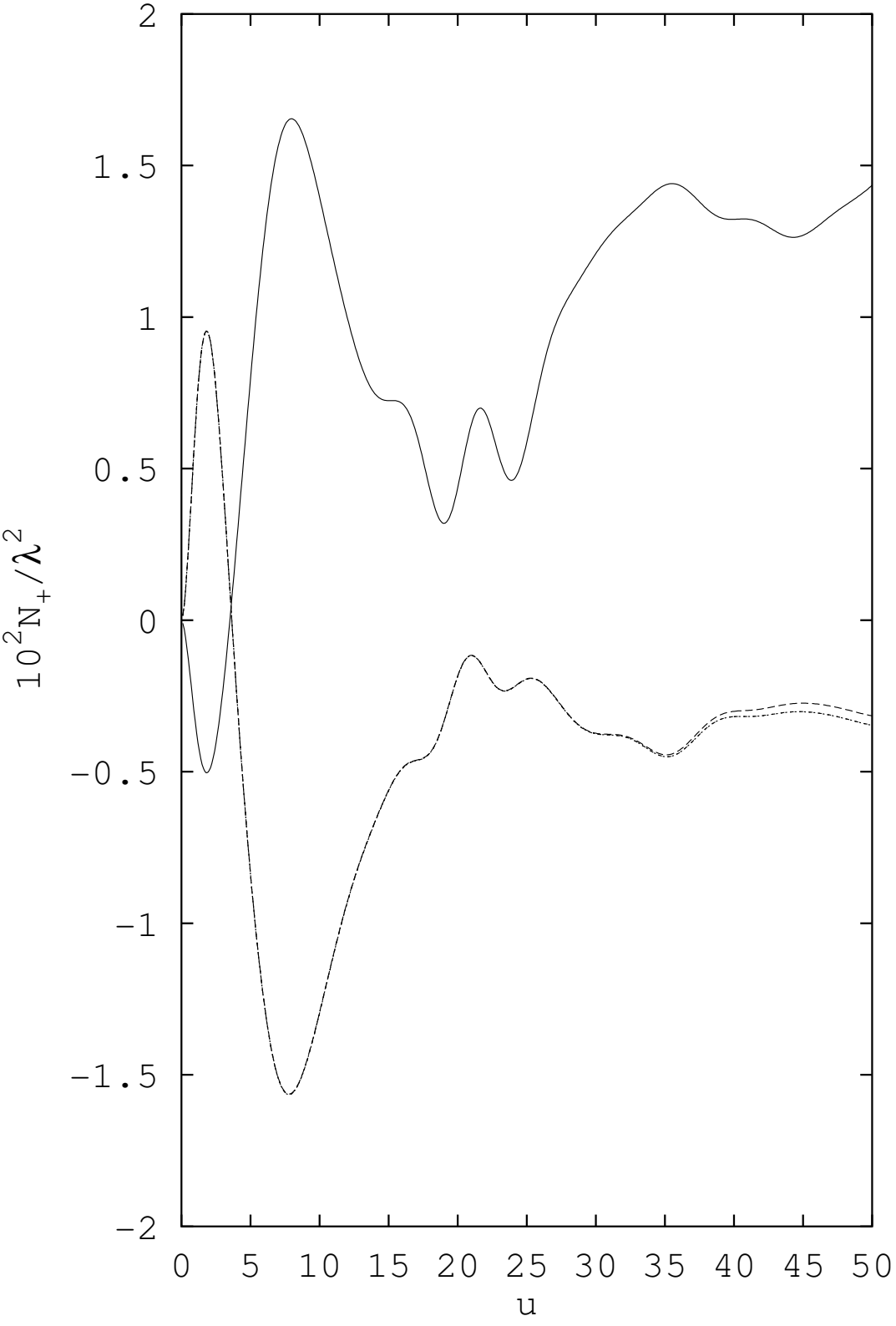

FIG. 9: $N_+(u)$ (multiplied by 10^2) is plotted for the $q = p = 0.5$ direction. The curves for $\lambda = 10^{-3}, 10^{-2}, 10^{-1}$ (broken line) overlap. For $\lambda = 10^{-12}$ (continuous line), numerical error breaks the expected quadratic scaling.

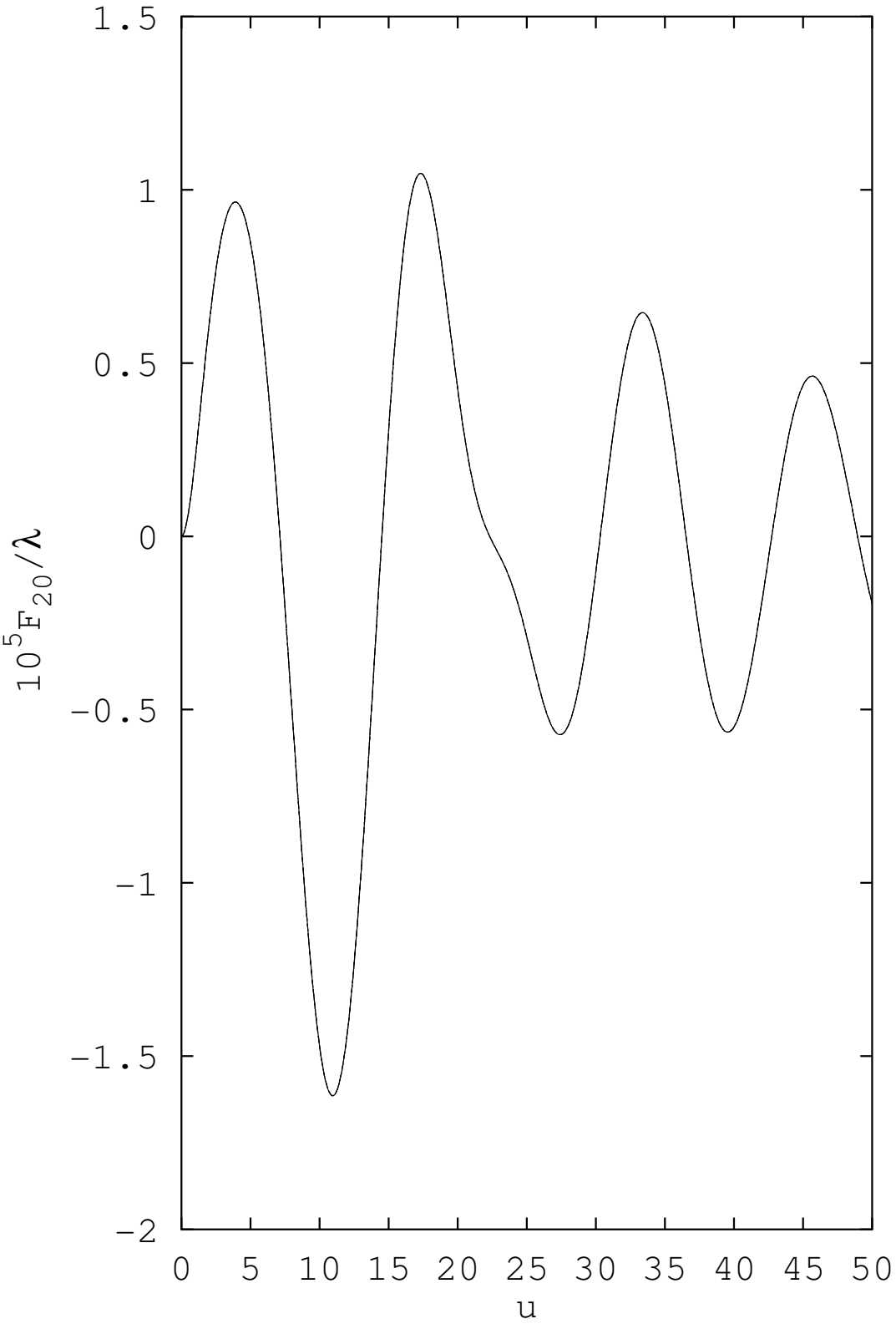

FIG. 10: The rescaled coefficient $F_{20}(u)/\lambda$ (multiplied by 10^5) is plotted for $\lambda = 10^{-12}, 10^{-3}, 10^{-2}, 10^{-1}$; all the curves overlap.

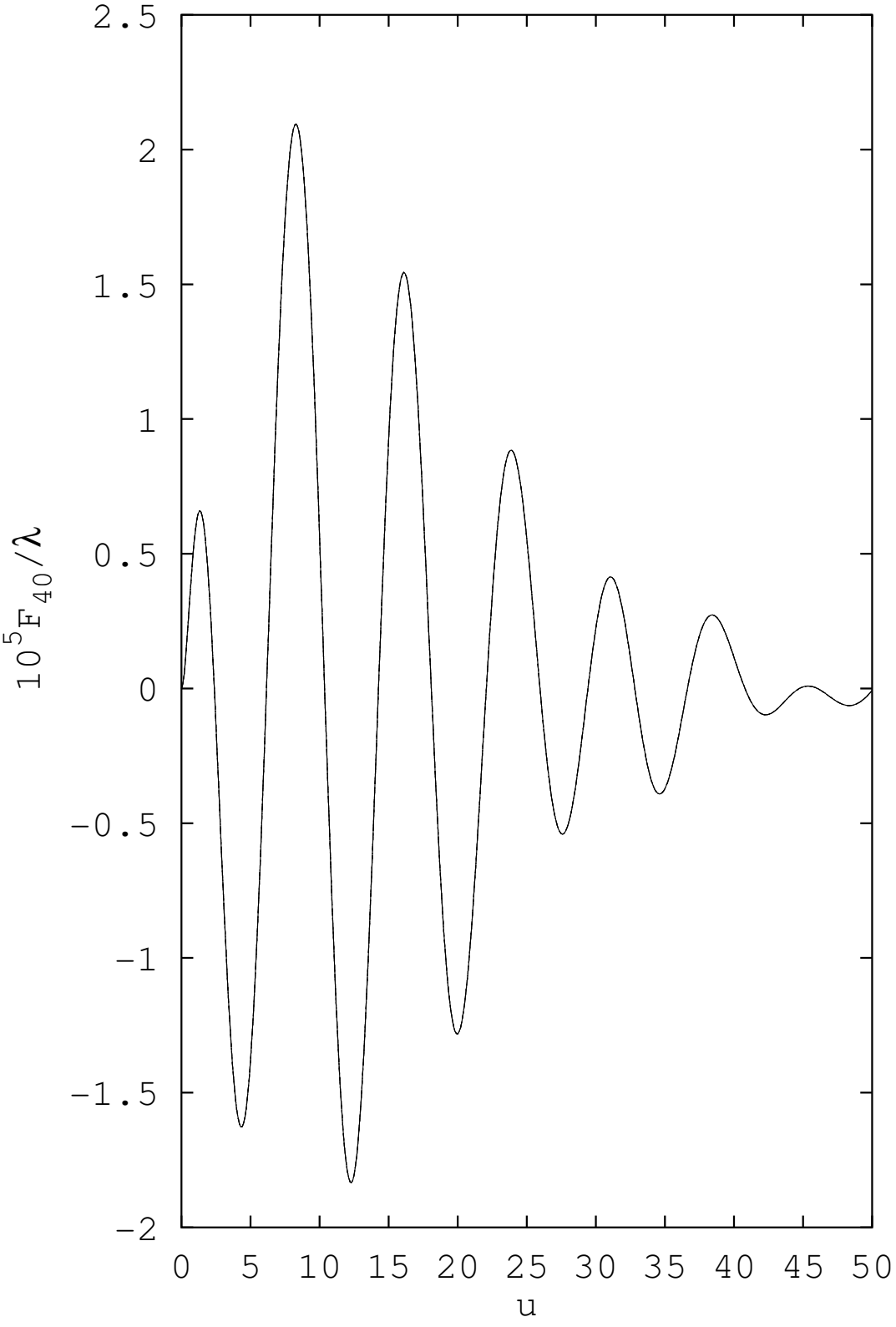

FIG. 11: The rescaled coefficient $F_{40}(u)/\lambda$ (multiplied by 10^5) is plotted for $\lambda = 10^{-12}, 10^{-3}, 10^{-2}, 10^{-1}$; all the curves overlap.

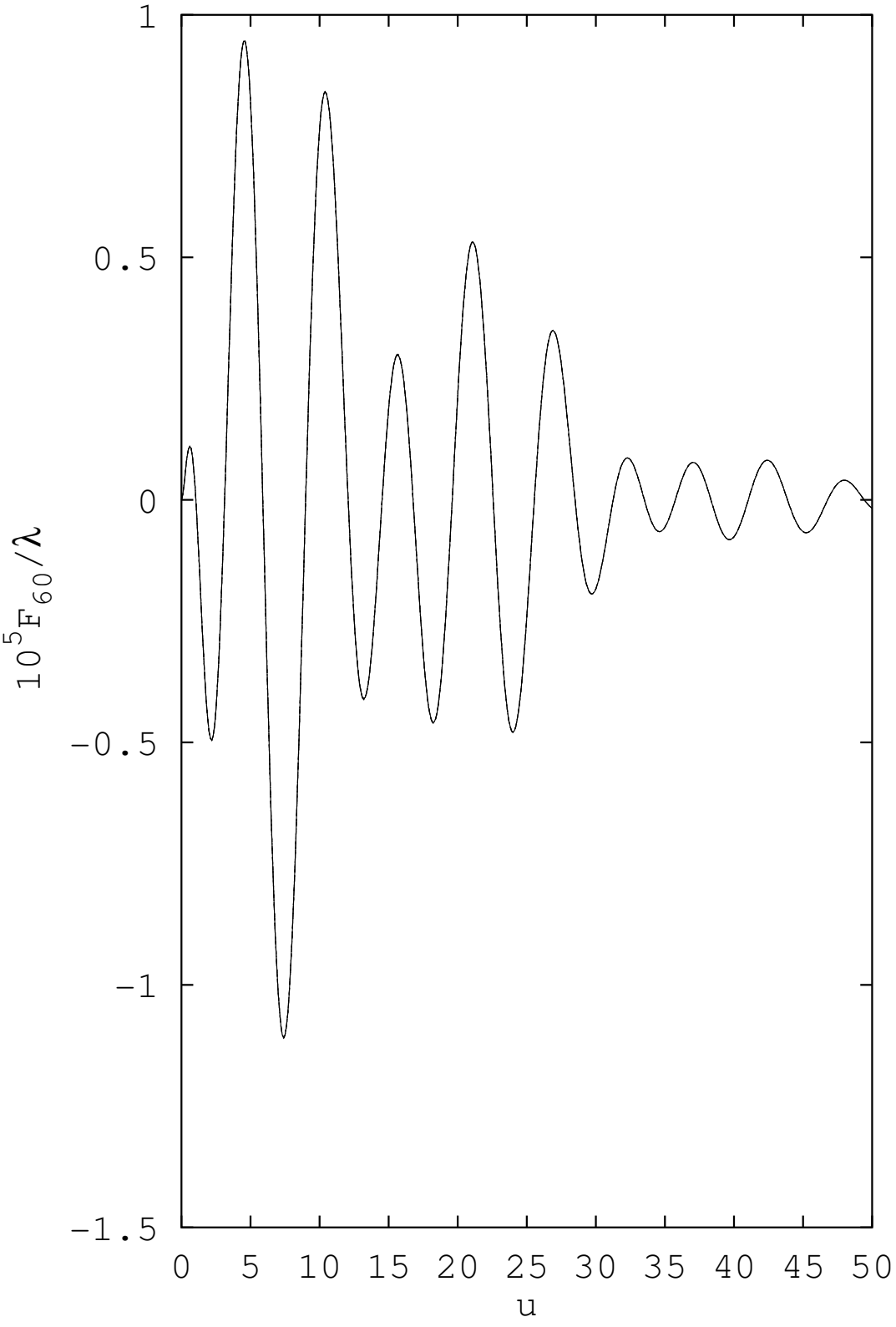

FIG. 12: The rescaled coefficient $F_{60}(u)/\lambda$ (multiplied by 10^5) is plotted for $\lambda = 10^{-12}, 10^{-3}, 10^{-2}, 10^{-1}$; all the curves overlap.

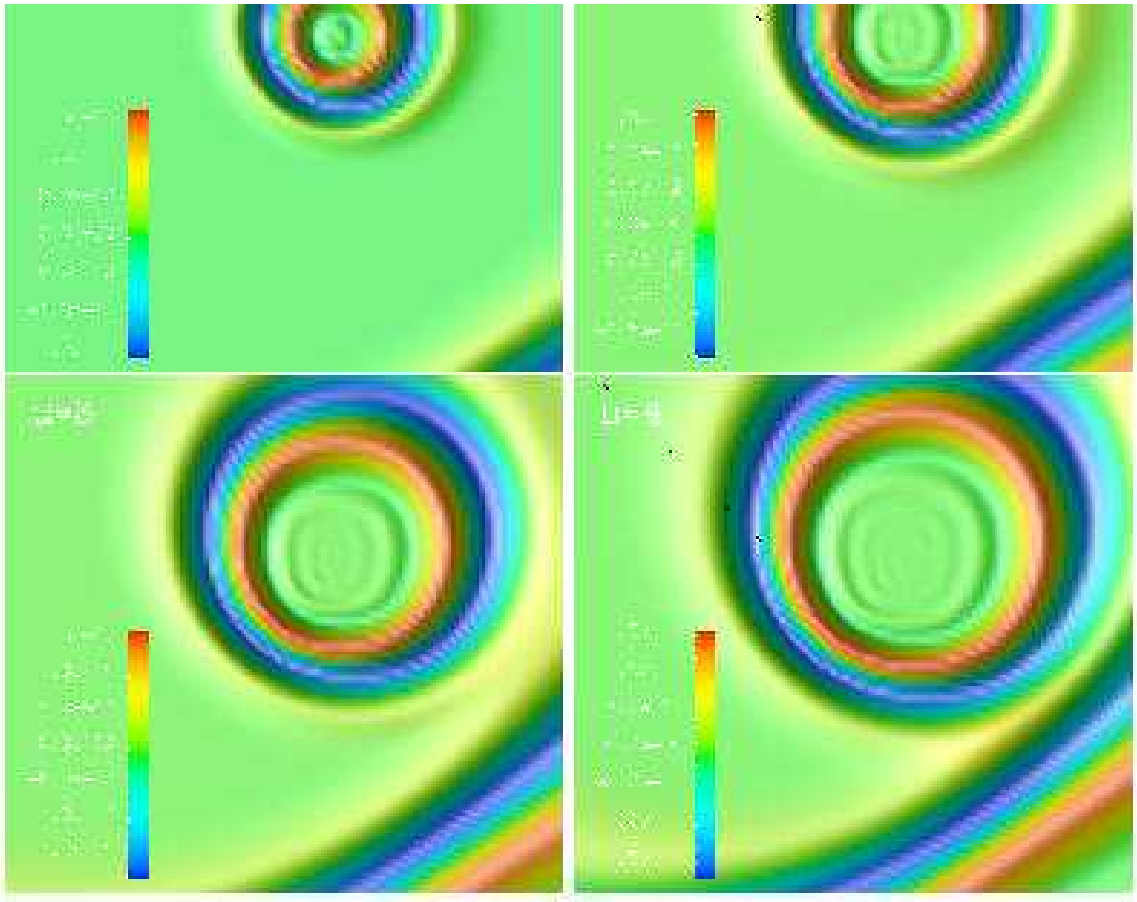

FIG. 13: Surface plots of $r\phi$ on the South patch of $\mathcal{I}^+$ for $u = 1, 2, 3, 4$, in zig–zag order from top to bottom, resulting from the scattering of an asymmetric pulse. The initial data parameters are $r_a = 3.5$, $r_b = 12$, $\lambda = 10^{-7}$, $\mu = 0.03$, $q_s = 0.2$, $p_s = 0.3$. The grid size is $85 \times 85 \times 101$.

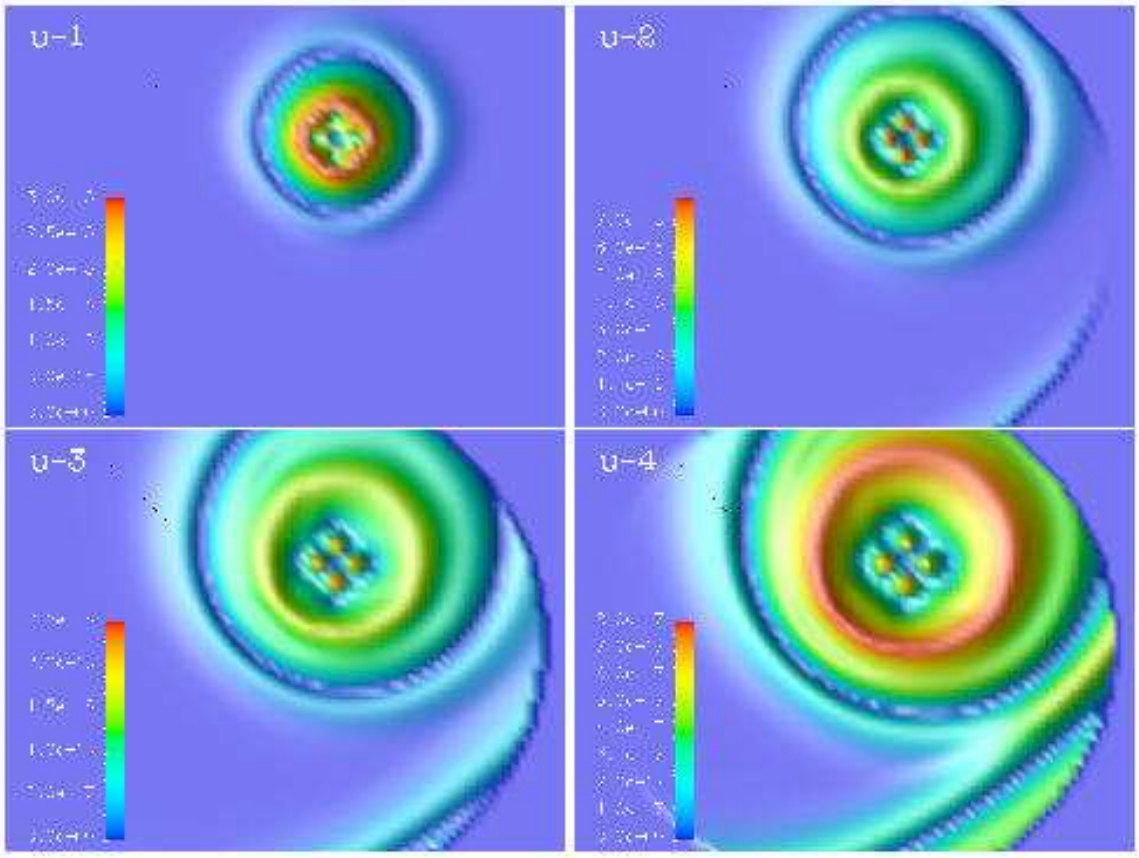

FIG. 14: Surface plots of the gravitational energy flux $|N|^2 = |N_+|^2 + |N_\times|^2$ on the South patch of $\mathcal{I}^+$ for $u = 1, 2, 3, 4$, in zig–zag order from top to bottom. The initial data parameters are $r_a = 3.5$, $r_b = 12$, $\lambda = 10^{-7}$, $\mu = 0.03$, $q_s = 0.2$, $p_s = 0.3$. The grid size is $85 \times 85 \times 101$. The maximum value of $|N|$ is of order 10^{-15}.